

ARTICLE

<https://doi.org/10.1038/s43246-019-0005-6>

OPEN

Design of a multifunctional polar metal via first-principles high-throughput structure screening

Yue-Wen Fang^{1,2*} & Hanghui Chen ^{2,3*}

Intrinsic polar metals are rare, especially in oxides, because free electrons screen electric fields in a metal and eliminate the internal dipoles that are needed to break inversion symmetry. Here we use first-principles high-throughput structure screening to predict a new polar metal in bulk and thin film forms. After screening more than 1000 different crystal structures, we find that ordered $\text{BiPbTi}_2\text{O}_6$ can crystallize in three polar and metallic structures, which can be transformed between via pressure or strain. In a heterostructure of layered $\text{BiPbTi}_2\text{O}_6$ and PbTiO_3 , multiple states with different relative orientations of $\text{BiPbTi}_2\text{O}_6$ polar displacements, and PbTiO_3 polarization, can be stabilized. At room temperature, the interfacial coupling enables electric fields to first switch PbTiO_3 polarization and subsequently drive 180° change of $\text{BiPbTi}_2\text{O}_6$ polar displacements. At low temperatures, the heterostructure provides a tunable tunnelling barrier and might be used in multi-state memory devices.

¹Department of Materials Science and Engineering, Kyoto University, Kyoto, Japan. ²NYU-ECNU Institute of Physics, New York University Shanghai, Shanghai, China. ³Department of Physics, New York University, New York, USA. *email: fyuewen@gmail.com; hanghui.chen@nyu.edu

Polar metals—analogy of ferroelectrics in metals—are characterized by intrinsic conduction and inversion symmetry breaking. Polar metals are rare (especially in oxides) because mobile electrons screen electric fields in a metal and eliminate internal dipoles that are needed to break inversion symmetry. The discovery of LiOsO_3 ¹, a metal that transforms from a centrosymmetric $R3c$ structure to a polar $R3c$ structure at 140 K, has stimulated an active search for new polar metals in both theory and experiment^{2–9}.

Density-functional-theory-based first-principles calculations have proven accurate in describing crystal structures and have been successfully applied to predict new functional materials, such as ferroelectrics, piezoelectrics and multiferroics¹⁰. Since crystal structure is the essential property of polar metals, we need to scrutinize the prediction by not presupposing an a priori favorable crystal structure. First-principles high-throughput crystal structure screening method, which is based on the marriage between first-principles calculations and a multitude of techniques such as particle-swarm optimization algorithm¹¹ and evolutionary algorithm¹², has demonstrated its superior power in effectively searching for the ground state structures and metastable structures of functional materials with only the given knowledge of chemical composition^{13–15}.

In this work, we use ab initio high-throughput structure screening to predict a new polar metal $\text{BiPbTi}_2\text{O}_6$ (BPTO for short). After screening over 1000 different crystal structures, we find that ordered BPTO can crystallize in three different polar metallic structures (post-perovskite $Pmm2$, perovskite $Pmm2$ and perovskite $Pmn2_1$), each of which can be transformed to another via external pressure or epitaxial strain. The mechanism is that 6s lone-pair electrons of Bi and Pb ions tend to favor off-center displacements¹⁰. On the other hand, in the perovskite structures, Bi^{3+} and Pb^{2+} enforce a fractional valence on Ti, which leads to conduction; in the post-perovskite structure, strong hybridization between Bi/Pb 6p and O 2p states induces a finite density of states at the Fermi level.

Next we demonstrate potential applications of the new polar metal BPTO by studying a BPTO/ PbTiO_3 heterostructure. We find that different states in which BPTO polar displacements are

parallel, anti-parallel and perpendicular to PbTiO_3 polarization can be stabilized in the heterostructure. Also, 180° switching of BPTO polar displacements needs to surmount an energy barrier of about 58 meV per slab. This implies that at room temperature where thermal fluctuations can overcome the switching barrier, the interfacial coupling between the polarization and polar displacements enables an electric field to first switch PbTiO_3 polarization and subsequently drive BPTO to change its polar displacements by 180° ; at low temperatures where the switching barrier dominates over thermal fluctuations, the BPTO polar displacements can not be switched but the direction of PbTiO_3 polarization can be controlled by an electric field. This can stabilize three distinct states with different tunnelling barriers.

Results and discussion

Most stable crystal structures of bulk BPTO. The key question in predicting a new polar metal is to determine its crystal structure. Since ordered BPTO has not been synthesized in experiment, we perform a first-principles high-throughput search for the ground state structure using CALYPSO^{11,16} method, in combination with CrySPY¹⁷. In the search, we do not constrain ourselves in any a priori favorable crystal structure. We screen >1000 different crystal structures among which we consider different Bi/Pb ordering in perovskite structure: layered ordering, columnar ordering and rock-salt ordering; and we also consider many non-perovskite structures, including post-perovskite structure and hexagonal structure. The computational details of our first-principles calculations and high-throughput structure screening method are provided in Methods.

Figure 1 shows ten lowest-energy crystal structures of BPTO from our calculations. The details of these ten crystal structures are available in Supplementary Table 1. The lowest energy structure is post-perovskite with a polar symmetry $Pmm2$ (space group No. 25). The crystal structure is explicitly shown in Fig. 1b. The TiO_6 octahedra are both corner-sharing and edge-sharing. The lack of inversion symmetry can be appreciated from Ti atoms which have strong polar displacements with respect to neighboring O atoms towards x -axis. The next two lowest-energy crystal

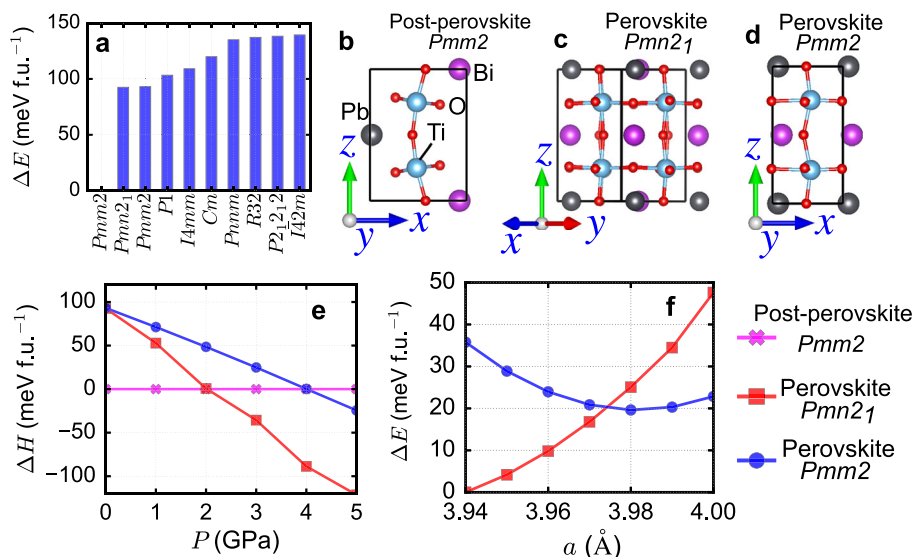


Fig. 1 The lowest-energy crystal structures and phase transitions. **a** Ten lowest-energy crystal structures of BPTO predicted by CALYPSO and DFT calculations. **b** Post-perovskite $Pmm2$ structure; **c** Perovskite $Pmn2_1$ structure; **d** Perovskite $Pmm2$ structure. **e** Enthalpy of the three lowest-energy structures as a function of pressure. The enthalpy of the post-perovskite $Pmm2$ structure under each pressure is set as the zero point. **f** Total energy of the two lowest-energy perovskite structures as a function of epitaxial strain. The energy of the perovskite $Pmn2_1$ structure constrained by an in-plane lattice constant of 3.94 \AA is chosen as the zero energy.

structures are both perovskite with $Pmn2_1$ symmetry (space group No. 31) and $Pmm2$ symmetry (space group No. 25). Both $Pmn2_1$ and $Pmm2$ symmetries are polar. The two perovskite structures have almost the same energy. Figure 1c shows the perovskite $Pmn2_1$ crystal structure. Bi and Pb atoms form a rock-salt ordering and their displacements with respect to O atoms in the xy plane make the crystal structure acentric. Figure 1d shows the perovskite $Pmm2$ crystal structure. Bi and Pb atoms have a layered ordering with a stacking direction along z -axis. It is clear that Bi, Pb, and Ti atoms all have strong polar displacements with respect to O atoms along x -axis, which breaks inversion symmetry. While post-perovskite oxides are interesting by themselves^{18,19}, perovskite oxides have been widely studied and are more suitable for device applications because many perovskite oxide substrates are available²⁰, which makes it feasible to grow perovskite oxide thin films. Therefore, we consider using external pressure or epitaxial strain to transform BPTO among different polar structures. Pressure is widely used in bulk synthesis to isolate metastable phases of matter^{21,22}. Figure 1e shows that both perovskite $Pmn2_1$ and $Pmm2$ structures become more stable than the post-perovskite $Pmm2$ structure under a few GPa. The reason is that the post-perovskite $Pmm2$ structure is very hollow with a very large volume of $130 \text{ \AA}^3 \text{ f.u.}^{-1}$ under ambient conditions, while the two perovskite structures are more closely packed ($122 \text{ \AA}^3 \text{ f.u.}^{-1}$ and $126 \text{ \AA}^3 \text{ f.u.}^{-1}$ under ambient conditions, respectively). Applying pressure favors structures with smaller volumes. If we want to grow BPTO thin films on a perovskite oxide substrate, the post-perovskite structure does not form due to very large lattice mismatch (see Supplementary Table 1 for the cell parameters of post-perovskite structure). The pseudo-cubic lattice constant of the perovskite $Pmn2_1$ structure is 3.94 \AA , while that of the perovskite $Pmm2$ structure is 3.98 \AA . It is anticipated that as the substrate lattice constant varies from 3.94 \AA to 3.98 \AA , the energetically favored structure changes from the perovskite $Pmn2_1$ structure to the perovskite $Pmm2$ structure. This is indeed what Fig. 1f shows. Since the perovskite $Pmm2$ structure has a layered ordering of Bi/Pb atoms, it is highly suitable for thin film growth methods such as pulsed layer deposition and molecular beam epitaxy²³. Substrates such as NdScO_3 and KTaO_3 have a proper lattice constant to stabilize the perovskite $Pmm2$ structure in BPTO thin films. The DFT calculated lattice constants of KTaO_3 and NdScO_3 can be found in Supplementary Table 2 with the comparison to the experimental data. We also enforce the post-perovskite $Pmm2$ structure to be stabilized on a perovskite oxide substrate and we expectedly find that its total energy is about 10 eV f.u.^{-1} higher than the two perovskite structures because of the large lattice mismatch (Supplementary Fig. 1). In addition to the study of phase transitions under strains and pressures, the temperature effect on phase transitions can be found in Supplementary Fig. 2.

Electronic and magnetic properties of polar metal BPTO. The upper panels of Fig. 2 show the DFT-calculated densities of states of the post-perovskite $Pmm2$, perovskite $Pmn2_1$ and perovskite $Pmm2$ structures. We calculate both total density of states (DOS) and orbital-projected DOS (Ti-3d, Bi-6s, Pb-6s, and O-2p). In three optimized structures, we do not find any magnetization or charge disproportionation. Therefore spin-up and spin-down are summed in the DOS. The DOS projected on the two Ti atoms are identical and hence are also summed. The three DOS share similarities but also have important differences. All three structures have a non-zero DOS at the Fermi level; both Bi-6s and Pb-6s are well below the Fermi level and are fully occupied. The difference is that in both perovskite structures ($Pmn2_1$ and $Pmm2$), because nominally Bi^{3+} , Pb^{2+} and O^{2-} , due to charge

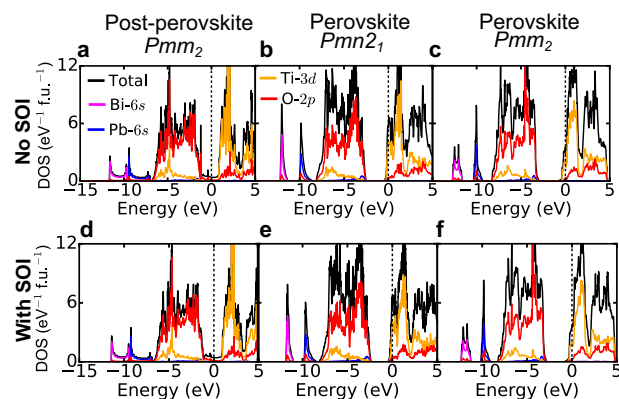


Fig. 2 Densities of states (DOS) of BPTO of the three polar structures.

The upper and lower panels show the DOS calculated by DFT without spin-orbit interactions (SOI) and DFT with SOI, respectively. **a, d** The post-perovskite structure with $Pmm2$ symmetry; **b, e** The perovskite structure with $Pmn2_1$ symmetry; **c, f** The perovskite structure with $Pmm2$ symmetry. The black curve is the total DOS. The magenta, blue, orange, and red curves are Bi-6s, Pb-6s, Ti-3d, and O-2p projected DOS, respectively. The dashed line is the Fermi level.

Table 1 Bader charges for bulk BPTO.

Structural type	Space group	Bader charges (e)			
		Bi	Pb	Ti	O
Post-perovskite	$Pmm2$	+1.48	+1.13	+2.19	-1.16
Perovskite	$Pmn2_1$	+1.73	+1.35	+2.12	-1.22
Perovskite	$Pmm2$	+1.73	+1.32	+2.06	-1.19

Charges are normalized to per atom

neutrality Ti must have a formal valence of $\text{Ti}^{3.5+}$, i.e., every Ti atom has 0.5 electron in the 3d conduction bands (no charge disproportionation is found in the calculations). Figure 2b, c shows that the Fermi level crosses Ti-3d states in the DOS of the perovskite $Pmn2_1$ and $Pmm2$ structures. However, in the post-perovskite structure (Fig. 2a), Ti-3d states have negligible contribution around the Fermi level. Instead, Bi-6p and Pb-6p, as well as O-2p states make the largest contribution to the DOS around the Fermi level, which can also be seen in Supplementary Fig. 3 where the electronic states around the Fermi level are zoomed in.

The Bader (static) charge analysis in Table 1 shows that Bi and Pb have about 0.25 and 0.19 more electrons in the post-perovskite structure than in the perovskite structures, which indicates stronger hybridization between Bi/Pb and O atoms in the post-perovskite structure. Therefore in the post-perovskite structure, Bi-6p and Pb-6p states are not fully empty and thus appear around the Fermi level.

Pb and Bi are heavy elements and their spin-orbit interactions (SOI) are not negligible. In the lower panels of Fig. 2, we take into account SOI and show the corresponding densities of states of BPTO of the three polar structures. Similar to the results without SOI, we do not find any magnetization or charge disproportionation in the fully relaxed structures. By comparing the densities of states calculated by DFT without SOI (upper panels of Fig. 2) and DFT with SOI (lower panels of Fig. 2), SOI almost unaffected the electronic structure, similar to previous studies on other polar metals^{3,24}.

While DFT with/without SOI calculations do not find any magnetization or charge disproportionation, correlation effects from Ti-3d orbitals may favor spin ordering and charge ordering.

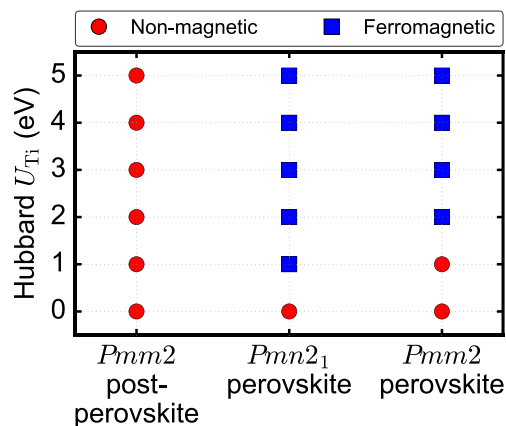


Fig. 3 Phase diagram as a function of Hubbard U . The magnetic phase diagram of the post-perovskite $Pmm2$, perovskite $Pmn2_1$ and perovskite $Pmm2$ structures as a function of Hubbard U_{Ti} . Non-magnetic state and ferromagnetic state are shown by red circle and blue square, respectively.

A long-range magnetic ordering with a charge disproportionation ($Ti^{3+} + Ti^{4+}$) can result in an insulating ground state²⁵. To test the robustness of our prediction that $BiPbTi_2O_6$ is a polar metal, we apply an effective Hubbard U correction on the Ti-3d orbitals and calculate the densities of states for all three low-energy structures. The accurate value of correlation strength of BPTO is not known, but presumably it should not exceed that of Mott insulator $LaTiO_3$, in which Hubbard U_{Ti} is about 5 eV²⁶. Therefore we consider a Hubbard U_{Ti} ranging from 0 to 5 eV. Within this range of U_{Ti} , we do not find charge disproportionation but find robust metallicity in all the three polar structures of BPTO. Furthermore, in this range of U_{Ti} , we find itinerant ferromagnetism in the perovskite $Pmn2_1$ structure at $U_{Ti} \geq 1$ eV and in the perovskite $Pmm2$ structure at $U_{Ti} \geq 2$ eV (antiferromagnetic ordering is less stable than ferromagnetic ordering). We do not find any magnetism in the post-perovskite $Pmm2$ structure up to $U_{Ti} = 5$ eV. The magnetic phase diagram for the three polar structures as a function of Hubbard U_{Ti} is shown in Fig. 3. The origin of itinerant ferromagnetism in BPTO is Stoner instability²⁷. In DFT+ U calculations, the Stoner criterion to induce itinerant ferromagnetism is²⁸:

$$U\rho(E_F) > 1, \quad (1)$$

where U and $\rho(E_F)$ are Hubbard U parameter and density of states at the Fermi level of a non-magnetic state, respectively. The upper panels of Fig. 2 shows that the perovskite $Pmn2_1$ structure has a large density of state at the Fermi level $\rho(E_F)$ in its non-magnetic state; the perovskite $Pmm2$ structure has a slightly smaller $\rho(E_F)$. Post-perovskite $Pmm2$ structure, on the other hand, has a very small $\rho(E_F)$ (9 times smaller than that of the perovskite $Pmm2$ structure and 15 times smaller than that of the perovskite $Pmn2_1$ structure). This explains that the critical U_{Ti} to stabilize itinerant ferromagnetism in the perovskite $Pmn2_1$ structure is the smallest, while a much larger U_{Ti} (larger than 5 eV) is needed to induce magnetism in the post-perovskite $Pmm2$ structure.

The role of lone-pair electrons. A local structural instability arising from lone-pair electrons has been reported in ferroelectric insulators and degenerately doped ferroelectrics^{10,29–35}. However, lone-pair electrons alone are not sufficient to stabilize a polar state in metals nor a ferroelectric state in insulators. For example, $BiFeO_3$ is ferroelectric³⁰ but $BiMnO_3$ is anti-ferroelectric^{36,37} although lone-pair electrons are present in both of them. Therefore, high-throughput crystal structure prediction is essential in predicting new polar metals and ferroelectric insulators.

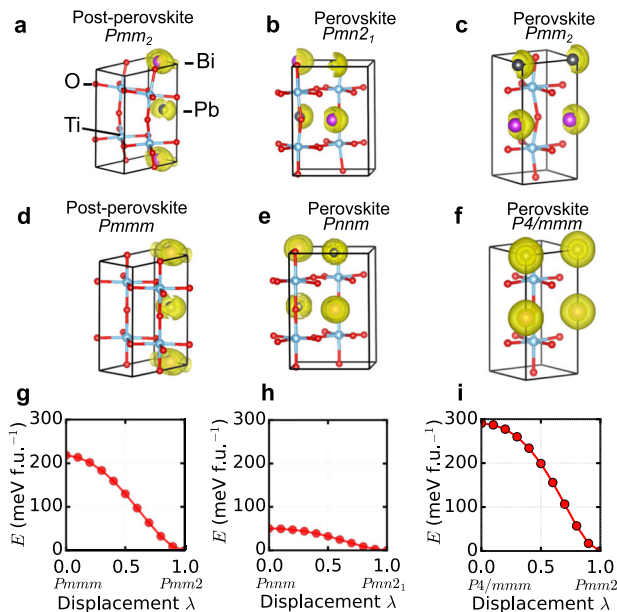


Fig. 4 Electron localization function (ELF) and the energy curve from the centrosymmetric structure to the corresponding polar structure. **a** The polar structure: post-perovskite $Pmm2$ and **d** the centrosymmetric structure: post-perovskite $Pmmm$; **b** The polar structure: perovskite $Pmn2_1$ and **e** the centrosymmetric structure: perovskite $Pnmm$; **c** The polar structure: perovskite $Pmm2$ and **f** the centrosymmetric structure: perovskite $P4/mmm$. The isosurface of ELF is set at a value of -0.5 . **g** Transition from the post-perovskite $Pmmm$ structure to the post-perovskite $Pmm2$ structure. **h** Transition from the perovskite $Pnmm$ structure to the perovskite $Pmn2_1$ structure. **i** Transition from the perovskite $P4/mmm$ structure to the perovskite $Pmm2$ structure.

In our study, the crystal structure screening takes into account both polar and anti-polar states for different cation orderings.

We now show that in the three lowest-energy metallic phases of BPTO, the lone-pair 6s electrons in Bi and Pb play an important role in breaking inversion symmetry. We use electron localization function (ELF, defined in Methods) to explicitly visualize how lone-pair electrons of Bi and Pb break inversion symmetry in metallic BPTO. Figure 4a–c shows an iso-surface of ELF of the three polar structures of BPTO. Only the ELF of Bi and Pb ions are displayed for clarity. Similar to insulating Bi-based and Pb-based perovskite oxides^{29,30,38}, the ELF shows that a lobe-like lone-pair resides on one side of Bi and Pb ions in all three polar metallic structures, which is the driving force to break inversion symmetry. On the other hand, ELF in the corresponding centrosymmetric structures shows spherical-symmetric feature, which is implied in Fig. 4d–f. Furthermore, we calculate the total energy variation as a function of normalized polar displacement λ from the centrosymmetric structures to the polar structures (see Fig. 4g–i). In all three cases, the energy curve monotonically decreases from the centrosymmetric structure to the polar structure, which indicates a continuous and spontaneous phase transition below a critical temperature (satisfying Anderson's and Blount's criterion of a ferroelectric-like metal³⁹). The energy difference between the polar structure and the corresponding centrosymmetric structure of BPTO in all three cases is larger than that of $LiOsO_3$ (about 25 meV f.u.⁻¹), implying that the structural transition temperature of BPTO is higher than that of $LiOsO_3$ ⁴⁰. We note that the above second-order structural phase transition is a key property to distinguish intrinsic polar metals from degenerately doped ferroelectrics^{32–35,41,42}, because realistic dopants (cation substitution or oxygen vacancies) make the

crystal symmetry of doped ferroelectrics ill-defined and correspondingly there is no well-defined continuous structural phase transition at finite temperatures.

Switching barrier of BPTO thin films in a heterostructure.

Next we study BPTO thin films. The $Pmm2$ perovskite structure of BPTO, which has a layered Bi/Pb ordering, is highly suitable for thin film growth and can be stabilized on a perovskite oxide substrate having a lattice constant of 3.98 Å or larger. The Bi/Pb stacking direction in the $Pmm2$ perovskite structure is chosen as the z -axis, while the polar displacements are in the xy -plane. In addition, we find that constrained by an in-plane lattice constant of 3.98 Å or larger, ferroelectric $PbTiO_3$ is under tensile strain and favors an in-plane polarization over an out-of-plane polarization (Supplementary Fig. 4). Therefore, we study a BPTO/ $PbTiO_3$ heterostructure, in which both BPTO polar displacements and $PbTiO_3$ polarization are parallel to the interface. We will show that different from previously studied ferroelectric/polar-metal heterostructures^{2,4,43,44}, multiple states with different relative orientations of $BiPbTi_2O_6$ polar displacements and $PbTiO_3$ polarization can be stabilized. When an electric field is applied to switch the polarization of $PbTiO_3$, a finite energy barrier exists for BPTO to change its polar displacements by 180°. If the temperature is high enough that thermal fluctuations can overcome the energy barrier, the polar displacements of BPTO will follow the change of $PbTiO_3$ polarization. Otherwise, the polar displacements of BPTO stay put and form different configurations when the external electric field changes the direction of $PbTiO_3$ polarization.

Figure 5a shows a BPTO/ $PbTiO_3$ heterostructure. The in-plane lattice constant is constrained to 4 Å, which stabilizes both perovskite $Pmm2$ structure of BPTO and an in-plane polarization of $PbTiO_3$. Experimentally substrates such as $KTaO_3$ and $NdScO_3$ can provide such a lattice constant. Figure 5a shows two different configurations: on the left (right) is a “parallel state” (“anti-parallel state”) in which $PbTiO_3$ polarization is parallel (anti-parallel) to BPTO polar displacements. Both configurations are stabilized after relaxation in our calculations. We first find that one-unit-cell thin film of BPTO is still polar and metallic. Figure 5b shows layer-resolved conduction electrons by

integrating the partial density states of Ti- d orbitals (Supplementary Fig. 5). Conduction electrons are mainly confined in BPTO with some charge leakage into a few unit cells of $PbTiO_3$. This charge leakage is due to the proximate effect that Ti- d states in $PbTiO_3$ are empty while Ti- d states in BPTO nominally have 0.5e per Ti atom. Such a charge leakage can be effectively prevented by replacing $PbTiO_3$ with $PbTi_{1-x}Zr_xO_3$ ⁴⁵, which is supported by our calculations in Supplementary Fig. 6. Figure 5c shows the layer-resolved cation displacements of Ti and Pb/Bi with respect to O atoms along the x -axis. The polar displacements of Bi and Pb in BPTO are almost bulk-like in both configurations. We note that the polar property of BPTO is not due to the interfacial coupling with $PbTiO_3$ (Supplementary Fig. 7). With $PbTiO_3$ replaced by a paraelectric $SrTiO_3$ substrate, one-unit-cell BPTO layer still has polar displacements and is metallic (Supplementary Fig. 8).

Next we study thermodynamics and the energy barrier of switching between “parallel state” and “anti-parallel state”. DFT calculations find that the energy of “parallel state” is 37 meV per slab lower than that of “anti-parallel state”. This is because in “anti-parallel state”, a 180° domain wall is formed in $PbTiO_3$ close to the interface, which is clearly seen from Fig. 5c. Forming such a 180° domain wall in ferroelectrics increases energy^{46,47}. Figure 5c shows that in both configurations, the interface strongly favors a parallel coupling between BPTO polar displacements and $PbTiO_3$ polarization.

While “parallel state” is more stable than “anti-parallel state”, “anti-parallel state” can be stabilized by itself because it is a local minimum. Therefore a finite energy barrier exists for BPTO to 180° change its polar displacements from “anti-parallel state” to “parallel state”. To quantitatively calculate the energy barrier and identify a possible switching path for polar displacement, we perform the climbing image nudged elastic band (NEB) calculations⁴⁸ and use transition state theory⁴⁹. Transition state theory has been widely used in understanding polarization switching in ferroelectric thin films^{50,51}, as well as ferroelectric domain wall motion⁵². We choose “anti-parallel state” as the initial state and “parallel state” as the final state. We study a possible switching path in which BPTO polar displacements are 180° “rotated” in the xy plane. The NEB results are shown in Fig. 5d. Along the structural transition path from “anti-parallel

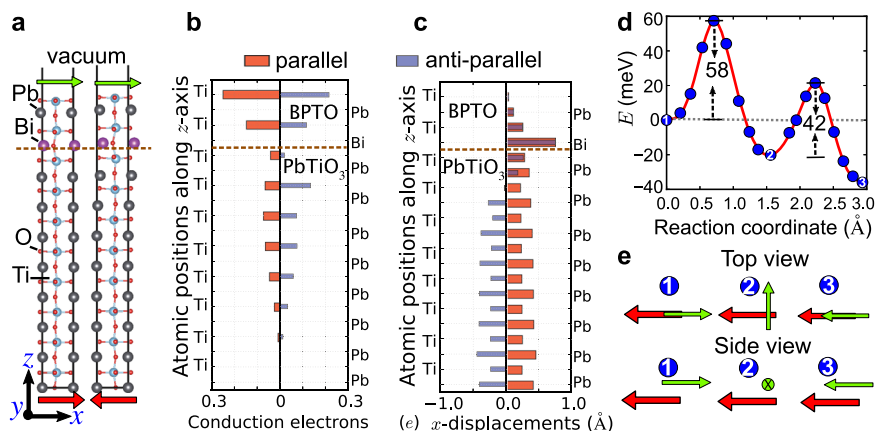


Fig. 5 Switching of polar displacements of BPTO in a BPTO/ $PbTiO_3$ heterostructure. **a** Atomic structure of the BPTO/ $PbTiO_3$ heterostructure: “parallel state” (left) and “anti-parallel state” (right). The red (green) arrow refers to $PbTiO_3$ polarization (BPTO polar displacement). **b** Layer-resolved conduction electrons on each Ti atom in parallel and anti-parallel states. **c** Layer-resolved polar displacements of metal ions along the x -axis in parallel and anti-parallel states. In **a**, **b** and **c**, the brown dashed lines indicate BPTO/ $PbTiO_3$ interface. **d** Calculated energy barrier along the transition path from the anti-parallel state to the parallel state. The energy of anti-parallel state is set as the zero point. The black dashed arrows highlight two energy barriers. The blue circles represent the images on the transition path found in the nudged elastic band calculations. The three energy minima along the transition path are schematically shown in **e**: “1” is the anti-parallel state, “3” is the parallel state and “2” is a metastable state with BPTO polar displacements perpendicular to $PbTiO_3$ polarization in the xy plane.

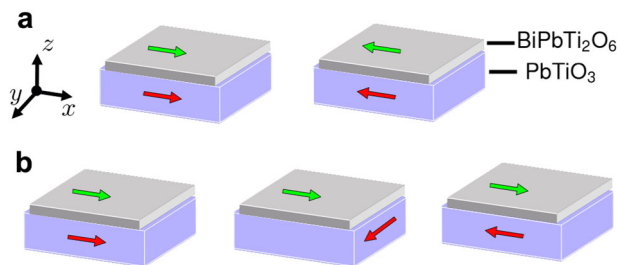


Fig. 6 Multifunctions of the BPTO/PbTiO₃ heterostructure. **a** At high temperature, the energy barrier is easily surmounted by thermal fluctuations and the polar displacements of BPTO can be switched. From the left panel to the right panel, as an electric field switches the polarization of PbTiO₃, the BPTO thin film follows the change and switches its polar displacements via the interfacial coupling. **b** At low temperature, the energy barrier can not be overcome and the polar displacements of BPTO get “stuck”. However, an electric field can switch the polarization of PbTiO₃ and stabilize multiple states with different orientation of PbTiO₃ polarization relative to the polar displacements of BPTO. Each state has different tunnelling barriers. From the left panel to the right panel, it is “parallel”, “perpendicular”, and “anti-parallel” state. The red arrow refers to the polarization of PbTiO₃ thin film. The green arrows refer to the polar displacements of BiPbTi₂O₆ thin film.

state” (labelled as “1”) to “parallel state” (labelled as “3”), there is another metastable state (labelled as “2”) where BPTO polar displacements are perpendicular to PbTiO₃ polarization in the *xy* plane (Fig. 5e). Between the three stable states (“1”, “2”, “3”), there are two energy barriers. The larger one, *i.e.*, the energy difference between the anti-parallel state and the highest saddle point, is 58 meV per slab.

Multifunctions of the BPTO/PTO heterostructure. In this section, we discuss potential functions of the BPTO/PTO heterostructure based on the calculated switching barrier in the previous section.

We first discuss room temperature applications. The switching barrier of BPTO is about 58 meV per slab. From transition state theory⁴⁹, at a given temperature *T*, an energy barrier ΔE with a magnitude of a few $k_B T$ can be easily surmounted [At room temperature, $1 k_B T \approx 26$ meV. In transition state theory, the probability *P* of overcoming the energy barrier is proportional to $e^{-\Delta E/k_B T}$, *i.e.*, $P \propto e^{-\Delta E/k_B T}$. The energy barrier ($\Delta E = 58$ meV) is about twice the $k_B T$, hence the probability of overcoming this barrier is around 14%.] (k_B is the Boltzmann constant). Room temperature $T = 300$ K is about 26 meV. Our energy barrier is about twice room temperature and therefore room temperature is sufficient to overcome the barrier. This implies that the interfacial coupling at the BPTO/PbTiO₃ interface enables an electric field to first switch PbTiO₃ polarization and subsequently drive BPTO to 180° change its polar displacements. This realizes an electrically switchable bi-state in the new polar metal BPTO at room temperature. We note that the transition path chosen in the NEB calculation is only one possibility. The actual transition path could be different from the one in our study and the resulting energy barrier should be even lower, which will make the switching of BPTO polar displacements more feasible. Figure 6a schematically shows how we can use PbTiO₃ polarization to control the polar displacements of BPTO at room temperature.

The above switching mechanism is also applicable to multi-layer BPTO thin films. The mechanism is as follows. Our calculations find that bulk BPTO is more stable in the polar *Pmm2* perovskite structure than the anti-polar *Pmma* perovskite structure by 65 meV f.u.⁻¹. The anti-polar *Pmma*

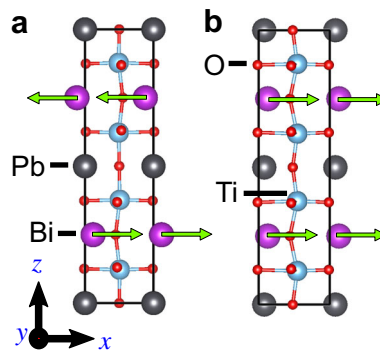


Fig. 7 The comparison between anti-polar and polar phases of BPTO. **a** The unit cell structure of anti-polar phase *Pmma* of BPTO. **b** The two unit cells structure of polar phase *Pmm2* of BPTO. The green arrows indicate the polar displacements of the Bi atoms.

perovskite structure is shown in Fig. 7a. The polar *Pmm2* perovskite structure is shown in Fig. 7b for comparison. Therefore, for multi-layer BPTO thin films, once the bottom layer of BPTO is 180° switched via the interfacial coupling, the remaining layers of BPTO will be driven by thermodynamics to change their polar displacements in a layer-by-layer manner to avoid an anti-polar state in the film. The above physical picture is computationally confirmed in Supplementary Fig. 9. However, for device applications (*e.g.* the model device illustrated in Supplementary Fig. 10), BPTO thin films of single-unit-cell thick are most desirable, in analogy to two-dimensional Van der Waals materials⁹.

Next we discuss low temperature applications. At sufficiently low temperatures where the energy barrier is much larger than $k_B T$, the interfacial coupling can not drive polar metals to change their polar displacements when an electric field switches the polarization of ferroelectrics. However, this has interesting implications: as we use the electric field to change the direction of PbTiO₃ polarization, we can individually stabilize multiple configurations in which the BPTO polar displacements are “parallel”, “perpendicular” and “anti-parallel” to the PbTiO₃ polarization (shown in Fig. 6b). Each configuration has different tunnelling resistance across ferroelectric insulators, because BPTO polar displacements and PbTiO₃ polarization have different relative orientation. As we use an electric field to change the direction of ferroelectric polarization (polar displacements do not follow due to low temperatures), we can tune tunnelling barriers between different states and therefore the BPTO/PbTiO₃ heterostructure can be used in multi-state memory devices.

In conclusion, we demonstrate the power of first-principles high-throughput screening in designing new functional materials and in particular predict a new polar metal BPTO by utilizing the Bi/Pb lone-pair electrons. The three lowest-energy structures of BPTO are all polar and metallic (post-perovskite *Pmm2*, perovskite *Pmm2* and perovskite *Pmn2₁*), which can be transformed among each other via pressure or strain. In the perovskite structures, Bi³⁺ and Pb²⁺ enforce a fractional valence 3.5+ on Ti, which leads to conduction. In the post-perovskite structure, strong hybridization between Pb/Bi *6p* and O *2p* states induces a finite density of states at the Fermi level. In a BPTO/PbTiO₃ heterostructures, at room temperature the interfacial coupling can overcome the switching barrier, which enables an electric field to first switch PbTiO₃ polarization and subsequently drive BPTO to 180° flip its polar displacements. This realizes an electrically switchable bi-state in the new polar metal BPTO. The switching method is applicable to other layered polar metals³. At low temperature, an electric field can control the direction of

PbTiO₃ polarization and stabilize multi states in which PbTiO₃ polarization and BPTO polar displacements have different relative orientations, implying different tunnelling resistance. This property can be used in tunable multi-state memory devices. We hope this work will stimulate experimentalists to synthesize the new polar metal in both bulk and thin-film forms.

Methods

First-principles calculations. For bulk structures, density functional theory (DFT) calculations are performed using a plane wave basis set and projector-augmented wave method⁵³, as implemented in the Vienna Ab-initio Simulation Package (VASP)^{54,55}. PBEsol, a revised Perdew–Burke–Ernzerhof (PBE) generalized gradient approximation for improving equilibrium properties of densely-packed solids⁵⁶, is used as the exchange correlation functional and has been applied successfully to interpreting the experimental observations of polar metal LiOsO₃ in our previous work²⁴. The Brillouin zone integration is performed with a Gaussian smearing of 0.05 eV over a Γ -centered k -mesh up to $12 \times 12 \times 12$ and a 600 eV plane-wave cutoff. The threshold of energy convergence is 10–6 eV. Hubbard U corrections are also considered in our calculations to model the effects of strong correlation on electronic and magnetic properties. The rotationally invariant approach of Hubbard U proposed by Dudarev et al.⁵⁷ is used in our DFT+ U calculations. Spin-orbit coupling (SOC) is also considered to study electronic structure in our DFT+ U +SOC calculations⁵⁸.

For the calculations of BPTO/PbTiO₃ structures, a Γ -centered k -mesh of $10 \times 10 \times 1$ is used. The periodic slabs are separated by vacuum of 20 Å thick to diminish the interaction between them. Since asymmetrical interface modelling is used in our calculations, we employ dipole correction to eliminate the artificial electric field in the vacuum^{59,60}. In all the interface calculations, the in-plane lattice constant is fixed to be 4 Å and the bottom layer of PbTiO₃ is fixed to simulate the bulk-like interior that is under tensile strain. All the other atoms are fully relaxed along the three axes. We consider two possible terminations of the heterostructure, i.e., BaO- and BiO-terminations. The former one is less stable than the latter one by ~220 meV per slab. Hence, we only report the BiO-terminated BPTO/PbTiO₃ interface in our study.

The energy barriers between the parallel and anti-parallel states, as well as the saddle points along the transition path are found by the nudged elastic band (NEB) calculations through the climbing image NEB method⁴⁸. In NEB calculations, a set of intermediate structures (i.e., images) between the initial state (anti-parallel state) and the final state (parallel state) are generated. They are iteratively adjusted so as to minimize the increase in energy along the transition path.

The electron localization function in our study, which is used to visualize lone-pair electrons in the real space is defined as⁶¹:

$$\text{ELF} = \left[1 + \left(\frac{D}{D_h} \right)^2 \right]^{-1} \quad (2)$$

where

$$D = \frac{1}{2} \sum_i |\nabla \phi_i|^2 - \frac{1}{8} \frac{|\nabla \rho|^2}{\rho} \quad (3)$$

and

$$D_h = \frac{3}{10} (3\pi^2)^{\frac{5}{3}} \rho^{\frac{5}{3}} \quad (4)$$

Here ρ is the electron density and ϕ_i are the Kohn–Sham wave functions.

Crystal structure search. The crystal structure search for bulk BPTO is carried out using the particle swarm optimization algorithm implemented in CALYPSO code^{11,16}, with the assistance of CrySPY¹⁷. More than 1000 structures (50% 10-atom BiPbTi₃O₆ and 50% 20-atom Bi₂Pb₂Ti₄O₁₂) are created in 20 generations. The structural optimization and computation of total energy are performed using VASP. In the first step of high-throughput screening of these 1000 crystal structure, we used non-spin polarized calculations with the exchange-correlation functional of PBEsol. The cutoff energy of 450 eV and the k -mesh grid density is about 2000 per atom. In the second step, the lowest 50 structures are re-calculated by the spin-polarized calculations in which the cutoff energy is increased to 600 eV and the k -mesh grid density is >2500 per atom. We consider ferromagnetic ordering and different types of antiferromagnetic orderings such as A-type, C-type and G-type⁶² to examine possible magnetic properties. The global structure search is performed under 0 GPa. The five lowest energy structures after screening are also studied under pressure. The space groups of the predicted crystal structures are examined by the FINDSYM code⁶³.

Visualization. We use software VESTA to show crystal structures and real-space electron localized functions⁶⁴.

Data availability

The authors declare that all the data supporting the findings of this study are available within the paper and its Supplementary Information.

Code availability

The high-throughput crystal structural predictions were carried out using the proprietary code VASP^{54,55}, with the combination of CALYPSO^{11,16} and CrySPY¹⁷. CALYPSO (<http://www.calypso.cn/>) is freely distributed on academic use under the license of Copyright Protection Center of China (registration No. 2010SR028200 and classification No. 61000-7500). CrySPY (<https://github.com/Tomoki-YAMASHITA/CrySPY>) is released under the Massachusetts Institute of Technology (MIT) License and is open source. The electronic structure calculations were all performed using VASP. The thermal properties are calculated by Phonopy⁶⁵. Phonopy (<https://github.com/atztogo/phonopy>) is released under the BSD-3-Clause License and is open source. The software VESTA⁶⁴ is distributed free of charge for academic users under the VESTA License (<https://jp-minerals.org/vesta/jp/download.htm>).

Received: 19 September 2019; Accepted: 3 December 2019;

Published online: 04 February 2020

References

- Shi, Y. et al. A ferroelectric-like structural transition in a metal. *Nat. Mater.* **12**, 1024–1027 (2013).
- Xiang, H. J. Origin of polar distortion in LiNbO₃-type “ferroelectric” metals: Role of A-site instability and short-range interactions. *Phys. Rev. B* **90**, 094108 (2014).
- Puggioni, D. & Rondinelli, J. M. Designing a robustly metallic noncentrosymmetric ruthenate oxide with large thermopower anisotropy. *Nat. Commun.* **5**, 3432 (2014).
- Filippetti, A., Fiorentini, V., Ricci, F., Delugas, P. & Íñiguez, J. Prediction of a native ferroelectric metal. *Nat. Commun.* **7**, 11211 (2016).
- Kim, T. et al. Polar metals by geometric design. *Nature* **533**, 68 (2016).
- Benedek, N. A. & Birol, T. ‘ferroelectric’ metals reexamined: fundamental mechanisms and design considerations for new materials. *J. Mater. Chem. C* **4**, 4000–4015 (2016).
- Luo, W., Xu, K. & Xiang, H. Two-dimensional hyperferroelectric metals: A different route to ferromagnetic-ferroelectric multiferroics. *Phys. Rev. B* **96**, 235415 (2017).
- Mochizuki, Y., Kumagai, Y., Akamatsu, H. & Oba, F. Polar metallic behavior of strained antiperovskites A CNiA (A = Mg, Zn, and Cd) from first principles. *Phys. Rev. Materials* **2**, 125004 (2018).
- Fei, Z. et al. Ferroelectric switching of a two-dimensional metal. *Nature* **560**, 336 (2018).
- Fang, Y.-W. et al. First-principles studies of multiferroic and magnetoelectric materials. *Sci. Bull.* **60**, 156–181 (2015).
- Wang, Y., Lv, J., Zhu, L. & Ma, Y. Calypso: a method for crystal structure prediction. *Comput. Phys. Commun.* **183**, 2063–2070 (2012).
- Glass, C. W., Oganov, A. R. & Hansen, N. USPEX-Evolutionary crystal structure prediction. *Comput. Phys. Commun.* **175**, 713–720 (2006).
- Wei, Y. et al. A rhombohedral ferroelectric phase in epitaxially strained Hf_{0.5}Zr_{0.5}O_{0.5} thin films. *Nat. Mater.* **17**, 1095–1100 (2018).
- He, J., Xia, Y., Naghavi, S. S., Ozoliņš, V. & Wolverton, C. Designing chemical analogs to PbTe with intrinsic high band degeneracy and low lattice thermal conductivity. *Nat. Commun.* **10**, 719 (2019).
- Zhao, Z. et al. Predicted pressure-induced superconducting transition in electride Li₆P. *Phys. Rev. Lett.* **122**, 097002 (2019).
- Wang, Y., Lv, J., Zhu, L. & Ma, Y. Crystal structure prediction via particle-swarm optimization. *Phys. Rev. B* **82**, 094116 (2010).
- Yamashita, T. et al. Crystal structure prediction accelerated by bayesian optimization. *Phys. Rev. Mater.* **2**, 013803 (2018).
- Murakami, M., Hirose, K., Kawamura, K., Sata, N. & Ohishi, Y. Post-perovskite phase transition in MgSiO₃. *Science* **304**, 855–858 (2004).
- Ohta, K. et al. The electrical conductivity of post-perovskite in earth’s D” layer. *Science* **320**, 89–91 (2008).
- Biswas, A., Yang, C.-H., Ramesh, R. & Jeong, Y. H. Atomically flat single terminated oxide substrate surfaces. *Prog. Surf. Sci.* **92**, 117–141 (2017).
- Zhang, Z. et al. High-pressure bulk synthesis of crystalline C₆N₉H₃-HCl: a novel C₃N₄ graphitic derivative. *J. Am. Chem. Soc.* **123**, 7788–7796 (2001).
- Klein, R. A. et al. High-pressure synthesis of the BiVO₃ perovskite. *Phys. Rev. Mater.* **3**, 064411 (2019).
- Korotcenkov, G. *Metal Oxide-based Thin Film Structures: Formation, Characterization and Application of Interface-based Phenomena*, (Elsevier, 2017).

24. Aulesti, E. I. P. et al. Pressure-induced enhancement of non-polar to polar transition temperature in metallic LiOsO₃. *Appl. Phys. Lett.* **113**, 12902 (2018).
25. Pentcheva, R. & Pickett, W. E. Correlation-driven charge order at the interface between a mott and a band insulator. *Phys. Rev. Lett.* **99**, 016802 (2007).
26. Pavarini, E. et al. Mott transition and suppression of orbital fluctuations in orthorhombic 3d¹ perovskites. *Phys. Rev. Lett.* **92**, 176403 (2004).
27. Fazekas, P. *Lecture notes on electron correlation and magnetism*, (World scientific, 1999).
28. Janicka, K., Velev, J. P. & Tsymbal, E. Y. Magnetism of LaAlO₃/SrTiO₃ superlattices. *J. Appl. Phys.* **103**, 07B508 (2008).
29. Cohen, R. E. Origin of ferroelectricity in perovskite oxides. *Nature* **358**, 136 (1992).
30. Ravindran, P., Vidy, R., Kjekshus, A., Fjellvåg, H. & Eriksson, O. Theoretical investigation of magnetoelectric behavior in BiFeO₃. *Phys. Rev. B* **74**, 224412 (2006).
31. Luo, W. & Xiang, H. Two-dimensional phosphorus oxides as energy and information materials. *Angew. Chem.* **128**, 8717–8722 (2016).
32. Zhao, H. J. et al. Meta-screening and permanence of polar distortion in metallized ferroelectrics. *Phys. Rev. B* **97**, 054107 (2018).
33. Gu, J.-x et al. Coexistence of polar distortion and metallicity in PbTi_{1-x}Nb_{1-x}O_{1-x}. *Phys. Rev. B* **96**, 165206 (2017).
34. He, X. & Jin, K.-j Persistence of polar distortion with electron doping in lone-pair driven ferroelectrics. *Phys. Rev. B* **94**, 224107 (2016).
35. Shen, X.-W., Fang, Y.-W., Tian, B.-B. & Duan, C.-G. Two-dimensional ferroelectric tunnel junction: the case of monolayer In:SnSe/SnSe/Sb:SnSe homostructure. *ACS Appl. Electron. Mater.* **1**, 1133–1140 (2019).
36. Baettig, P., Seshadri, R. & Spaldin, N. A. Anti-polarity in ideal BiMnO₃. *J. Am. Chem. Soc.* **129**, 9854–9855 (2007).
37. Goian, V. et al. Absence of ferroelectricity in BiMnO₃ ceramics. *J. Appl. Phys.* **112**, 074112 (2012).
38. Seshadri, R. & Hill, N. A. Visualizing the role of Bi 6s “lone pairs” in the off-center distortion in ferromagnetic BiMnOs. *Chem. Mater.* **13**, 2892–2899 (2001).
39. Anderson, P. W. & Blount, E. I. Symmetry considerations on martensitic transformations: “ferroelectric” metals? *Phys. Rev. Lett.* **14**, 217 (1965).
40. Wojdeł, J. C. & Íñiguez, J. Testing simple predictors for the temperature of a structural phase transition. *Phys. Rev. B* **90**, 014105 (2014).
41. Wang, Y., Liu, X., Burton, J. D., Jaswal, S. S. & Tsymbal, E. Y. Ferroelectric instability under screened coulomb interactions. *Phys. Rev. Lett.* **109**, 247601 (2012).
42. Xia, C., Chen, Y. & Chen, H. Coexistence of polar displacements and conduction in doped ferroelectrics: an ab initio comparative study. *Phys. Rev. Mater.* **3**, 054405 (2019).
43. Puggioni, D., Giovannetti, G. & Rondinelli, J. M. Polar metals as electrodes to suppress the critical-thickness limit in ferroelectric nanocapacitors. *J. Appl. Phys.* **124**, 174102 (2018).
44. Puggioni, D., Giovannetti, G., Capone, M. & Rondinelli, J. M. Design of a mott multiferroic from a nonmagnetic polar metal. *Phys. Rev. Lett.* **115**, 087202 (2015).
45. Zhang, Y. et al. Discovery of a magnetic conductive interface in PbZr_{0.2}Ti_{0.8}O₃/SrTiO₃ heterostructures. *Nat. Commun.* **9**, 685 (2018).
46. Li, M., Gu, Y., Wang, Y., Chen, L.-Q. & Duan, W. First-principles study of 180° domain walls in BaTiO_{180°}: Mixed Bloch-Néel-Ising character. *Phys. Rev. B* **90**, 054106 (2014).
47. Meyer, B. & Vanderbilt, D. Ab initio study of ferroelectric domain walls in PbTiO₃. *Phys. Rev. B* **65**, 104111 (2002).
48. Henkelman, G., Uberuaga, B. P. & Jónsson, H. A climbing image nudged elastic band method for finding saddle points and minimum energy paths. *J. Chem. Phys.* **113**, 9901–9904 (2000).
49. Laidler, K. J. & King, M. C. Development of transition-state theory. *J. Phys. Chem.* **87**, 2657–2664 (1983).
50. Tadmor, E., Waghmare, U., Smith, G. & Kaxiras, E. Polarization switching in PbTiO₃: an ab initio finite element simulation. *Acta Mater.* **50**, 2989–3002 (2002).
51. Wang, H. & Qian, X. Two-dimensional multiferroics in monolayer group IV monochalcogenides. *2D Mater.* **4**, 015042 (2017).
52. Li, X. Y. et al. Domain wall motion in perovskite ferroelectrics studied by the nudged elastic band method. *J. Phys. Chem. C* **122**, 3091–3100 (2018).
53. Blöchl, P. E. Projector augmented-wave method. *Phys. Rev. B* **50**, 17953–17979 (1994).
54. Kresse, G. & Furthmüller, J. Efficiency of ab-initio total energy calculations for metals and semiconductors using a plane-wave basis set. *Comp. Mater. Sci.* **6**, 15–50 (1996).
55. Kresse, G. & Furthmüller, J. Efficient iterative schemes for ab initio total-energy calculations using a plane-wave basis set. *Phys. Rev. B* **54**, 11169–11186 (1996).
56. Perdew, J. P. et al. Restoring the density-gradient expansion for exchange in solids and surfaces. *Phys. Rev. Lett.* **100**, 136406 (2008).
57. Dudarev, S. L., Botton, G. A., Savrasov, S. Y., Humphreys, C. J. & Sutton, A. P. Electron-energy-loss spectra and the structural stability of nickel oxide: an LSDA.U study. *Phys. Rev. B* **57**, 1505–1509 (1998).
58. Giovannetti, G. & Capone, M. Dual nature of the ferroelectric and metallic state in LiOsO₃. *Phys. Rev. B* **90**, 195113 (2014).
59. Makov, G. & Payne, M. C. Periodic boundary conditions in ab initio calculations. *Phys. Rev. B* **51**, 4014–4022 (1995).
60. Neugebauer, J. & Scheffler, M. Adsorbate-substrate and adsorbate-adsorbate interactions of Na and K adlayers on Al(111). *Phys. Rev. B* **46**, 16067–16080 (1992).
61. Silvi, B. & Savin, A. Classification of chemical bonds based on topological analysis of electron localization functions. *Nature* **371**, 683 (1994).
62. Ding, H.-C. & Duan, C.-G. Electric-field control of magnetic ordering in the tetragonal-like BiFeO₃. *EPL (Europhys. Lett.)* **97**, 57007 (2012).
63. Aroyo, M. I. et al. Crystallography online: Bilbao crystallographic server. *Bulg. Chem. Commun* **43**, 183–197 (2011).
64. Momma, K. & Izumi, F. VESTA 3 for three-dimensional visualization of crystal, volumetric and morphology data. *J. Appl. Crystallogr.* **44**, 1272–1276 (2011).
65. Togo, A. & Tanaka, I. First principles phonon calculations in materials science. *Scr. Mater.* **108**, 1–5 (2015).

Acknowledgements

We thank Kevin Garrity, Hongjun Xiang, and T. Yamashita for valuable discussions. We acknowledge support from National Natural Science Foundation of China (No. 11774236), Pujiang Talents program (No. 17PJ1407300), the Seed Grants of NYU-ECNU Joint Research Institutes and the 2019 University Research Challenge Fund. This research was carried out on the High Performance Computing resources at New York University New York, Abu Dhabi and Shanghai.

Author contributions

Y.-W.F. and H.C. designed the project, performed the calculations, analyzed the results, and wrote the manuscript.

Competing interests

The authors declare no competing interests.

Additional information

Supplementary information is available for this paper at <https://doi.org/10.1038/s43246-019-0005-6>.

Correspondence and requests for materials should be addressed to Y.-W.F. or H.C.

Reprints and permission information is available at <http://www.nature.com/reprints>

Publisher's note Springer Nature remains neutral with regard to jurisdictional claims in published maps and institutional affiliations.

 **Open Access** This article is licensed under a Creative Commons Attribution 4.0 International License, which permits use, sharing, adaptation, distribution and reproduction in any medium or format, as long as you give appropriate credit to the original author(s) and the source, provide a link to the Creative Commons license, and indicate if changes were made. The images or other third party material in this article are included in the article's Creative Commons license, unless indicated otherwise in a credit line to the material. If material is not included in the article's Creative Commons license and your intended use is not permitted by statutory regulation or exceeds the permitted use, you will need to obtain permission directly from the copyright holder. To view a copy of this license, visit <http://creativecommons.org/licenses/by/4.0/>.

© The Author(s) 2020